

UNIVERSITEIT VAN PRETORIA
UNIVERSITY OF PRETORIA
YUNIBESITHI YA PRETORIA

Low Temperature Thermal Properties of HTR Nuclear Fuel Composite Graphite.

by

PHATHUTSHEDZO MUROVHI

Submitted in partial fulfilment of requirements of degree of

Magister Scientiae

in the Department of Physics
in the Faculty of Natural and Agricultural Science

University of Pretoria,
Pretoria, South Africa

May, 2013

Promoter: Professor Ncholu Manyala

©University of Pretoria

Acknowledgments

I would like to express my sincere gratitude to the following people who have contributed towards the completion of this study:

- Prof. N Manyala for his guidance, advice, patience and mostly his understanding through this study and for giving me an opportunity to be part of this group.
- My colleagues in carbon chair for their support, advice and guidance.
- My mother for her patience, prayers, resolute support in tough times, advice and taking care of my son when I was busy during this study, finally we did it Mma.
- Fhatuwani Mushavhanamadi for his words of encouragement, endurance, support throughout this study you are my rock.
- Finally, I would like to thank my creator for giving me strength and motivation not to give up when things were tough and the only solution seems to be giving up.

Contributions

1. International Carbon conference 2011: Shangri
2. SAIP 2011: 52nd South African Institute of Physics conference (UNISA)
3. International Carbon Conference 2012: Poland, Krakow
4. SAIP 2012: 53rd South African Institute of Physics Conference (University of Pretoria)

Declaration

I, the undersigned, declare that the dissertation, which I hereby submit for the degree of Magister Scientae at the University of Pretoria is my own work and has not previously been submitted by me for any degree at this or any other tertiary institution.

.....

Phathutshedzo Murovhi

On this day of year.....

Dedication

I would like to fully dedicate this dissertation to my parents, my mother Avhaphani Elizabeth Murovhi, my late father Maluta Murovhi, my son Oritshidza Mushavhanamadi and my better half Fhatuwani Mushavhanamadi.

ACRONYMS

Cu	Copper
CVD	Chemical Vapour deposition
DFT	Density Functional Theory
FWHM	Full Width Half Maximum
HOPG	Highly Orientated Pyrolytic Graphite
HREM	High Resolution Electron Microscopy
HTR	High Temperature Reactor
IP	Instrumental
NG	Natural Graphite
OMDAQ	Oxford Micro-beams Data Acquisition System
PBMR	Pebble Bed Modular Reactor
PIXE	Proton Induced X-ray Emission
PPMS	Physical Property Measuring System
SG	Synthetic Graphite
SNICS	Source of Negative ions by Cesium Sputtering
SW	Stone Wale Defects
WPPM	Whole Powder Pattern Modelling
XRD	X-ray Diffraction

ABSTRACT

Graphite and graphite composite materials are of great importance in various applications; however, they have been widely used in nuclear applications. Primarily in nuclear applications such, as a moderator where its primary aim is to stop the fast neutrons to thermal neutron.

The composite graphite (HTR-10) has potential applications as a moderator and other applications including in aerospace field. Structurally the composite shows stable hexagonal form of graphite and no traces of the unstable Rhombohedral patterns. Thermal conductivity indicates the same trends observed and known for nuclear graded graphite.

The composite was made as a mixture of 64 wt% of natural graphite, 16 wt% of synthetic graphite binded together by 20 wt% of phenolic resin. The resinated graphite powder was uni-axially pressed by 19.5 MPa to form a disc shaped specimen. The disc was then cut and annealed to 1800 °C. The composite was further cut into two directions (parallel and perpendicular) to the pressing direction. For characterization the samples were cut into 2.5 x 2.5 x 10 mm³. There were exposed to proton irradiation for 3 and 4.5 hrs respectively and characterized both structurally and thermally.

Through the study what we have observed was that as the composite is exposed to proton irradiation there is an improvement structurally. Thus, the D peak in the Raman spectroscopy has decreased substantially with the irradiated samples. XRD has indicated that there is no un-stable Rhombohedral phase pattern in both the pristine and the irradiated samples.

However this was further confirmed with that thermal conductivity is also increasing with irradiation exposure. This is anomalous to irradiated graphite in which defects are supposedly induced. Looking into the electrical resistivity we have noted that pristine samples have higher resistivity as compared to the irradiated samples. Seebeck coefficient indicates that there is some form of structural perfection and the samples have a phonon drag dip at the known graphite temperature of 35 K. This has shown us there are no impurities induced by irradiation of the samples.

CONTENTS

ABSTRACT.....	VII
LIST OF FIGURES	X
LIST OF TABLES	XI
CHAPTER 1: INTRODUCTION.....	1
1.1 GENERAL INTRODUCTION	1
1.2 GRAPHITE APPLICATIONS IN NUCLEAR REACTORS	4
1.3 AIMS AND OBJECTIVES.....	5
References.....	6
CHAPTER 2: LITERATURE REVIEW	7
2.1 GRAPHITE	7
2.1.1 CRYSTAL STRUCTURE	7
2.1.2 PHYSICAL STRUCTURE	8
2.1.3 GRAPHITE COMPOSITES	10
2.2 IRRADIATION OF SOLIDS	12
2.2.2 RADIATION DEFECTS IN GRAPHITE	13
2.2.2.1 Interstitial Defects (Point Defects)	13
2.2.2.2 Interstitial Clusters.....	14
2.2.2.3 Vacancy Defects	14
2.2.2.4 Buckling and Folding Defects	15
2.2.3 EFFECTS OF RADIATION ON GRAPHITE.....	16
2.2.3.1 Structural Effects	16
2.2.3.2 Thermal Effects	16
References.....	19
CHAPTER 3: EXPERIMENTAL	21

3.1	MATERIALS	21
3.2	COMPOSITE PREPARATION METHOD.....	21
3.3	CHARACTERISATION TECHNIQUES.....	21
3.3.1	STRUCTURAL CHARACTERISATIONS	22
3.3.1.1	Raman Spectroscopy.....	22
3.3.1.2	X-Ray Diffraction (XRD)	23
3.3.2	THERMAL TRANSPORT MEASUREMENTS	24
3.3.2.1	Sample Preparation	25
3.3.2.2	Measurement Process Description.....	25
3.3.2.3	Thermal and Electrical Circuit	26
3.3.3	PROTON IRRADIATION.....	27
	References.....	28
CHAPTER 4: RESULTS AND DISCUSSION		29
4.1	STRUCTURAL CHARACTERISATION.....	29
4.1.1	RAMAN SPECTROSCOPY	29
4.1.2	X-RAY DIFFRACTION (XRD) PATTERN.....	30
4.2	THERMAL CHARACTERISATION	32
4.2.1	INTRODUCTION	32
4.2.2	THERMAL CONDUCTIVITY.....	34
4.2.2.1	Pristine Data	34
4.2.2.2	Irradiated Data.....	36
4.3	ELECTRICAL CHARACTERISATION	40
4.3.1	ELECTRICAL RESISTIVITY.....	40
4.3.2	SEEBECK COEFFICIENT.....	42
CHAPTER 5: CONCLUSION.....		44
	References.....	45

LIST OF FIGURES

Figure 1.1: Examples of carbon allotropes: (a) diamond, (b) graphite, (c) lonsdaleite, (d) C60, (e) C540 and (f) C70.....	1
Figure 1.2: The coating layers of fuel kernels into fuel spheres (pebbles).	4
Figure 2.1: Trigonal planar arrangement of sp^2 hybrid.....	7
Figure 2.2: Hexagonal graphene layers of bulk graphite	8
Figure 2.3: (a) Rhombohedral and (b) hexagonal crystal structure of graphite showing the stacking arrangement of the layers	9
Figure 3.1: Raman spectroscopy used for structural characterisation	22
Figure 3.2: The Bruker D8 Advanced XRD machine: (a) full view of the machine, and (b) closer view of the goniometer, the X-ray source, the sample holder/stage and the detector	23
Figure 3.3: The Quantum Design Physical Property Measuring System: (a) showing the operating system of the machine and (b) the sample holder (puck).....	24
Figure 3.4: Four-probe geometry of thermal and electrical connections	25
Figure 3.5: Van de Graaff scanning proton microscope used for irradiation of the samples: (a) indicates the part of the beam tube where the beam is channelled to the target and (b) shows the sample holder and the vacuum chamber in which the holder is inserted for measurements	27
Figure 4.1: Comparison of Raman spectra of pristine and irradiated samples for 3 and 4.5 h	29
Figure 4.2: X-ray diffraction (XRD) patterns for the graphite composite	30
Figure 4.3: Pristine total thermal, phonon and electronic conductivity of samples moulded at 19.5 MPa and measured (a) parallel and (b) perpendicular to the moulding pressure direction.....	35

LIST OF TABLES

Table 4.1: Average crystallite sizes along the basal plane and the degree of graphitisation of the high-pressure samples	31
Table 4.2: Comparison of l_3 calculated from equation 4.8 for the high-pressure samples	38
Table 4.3: Comparison of Residual Resistivity Ratio (RRR) for both low- and high-pressure samples	41

CHAPTER 1: INTRODUCTION

1.1 GENERAL INTRODUCTION

The word carbon is derived from the Latin *carbo*, meaning coal. Carbon is classified as a non-metallic element with $1s^2 2s^2 2p^2$ electronic configuration. This electronic configuration allows carbon to have a tetravalent bonding ability in addition to four probable hybridisation states, sp^1 , sp^2 and sp^3 . The sp^2 hybridisation state forms the basis of all graphitic materials, whereas the sp^3 hybridisation state governs diamond structures. Furthermore, carbon is vastly regarded scientifically, including in engineering applications, for its bonding properties and its several allotropes have vast applications. These allotropes include, *inter alia*, diamond, graphite and amorphous carbon. Graphite and diamond are the most valued allotropes. Figure 1.1 presents a few of these allotropes.

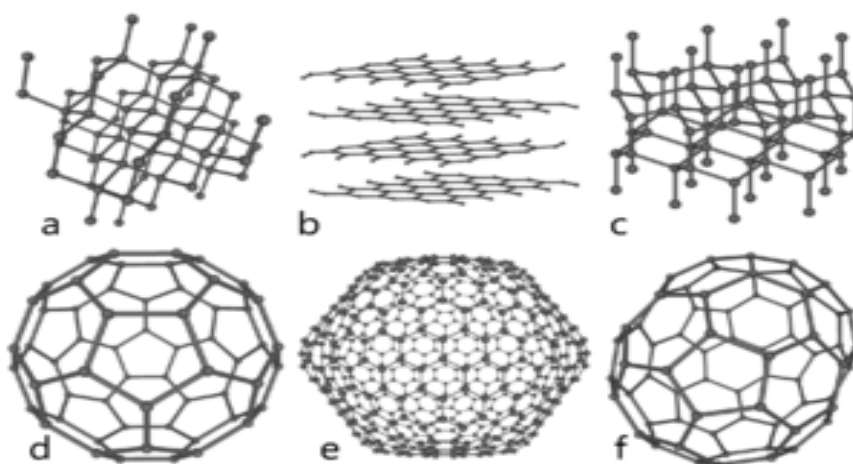


Figure 1.1: Examples of carbon allotropes: (a) diamond, (b) graphite, (c) lonsdaleite, (d) C₆₀, (e) C₅₄₀ and (f) C₇₀

The graphite allotrope was discovered around 1987 by Abraham Gottlob Werner. He named it allotrope from the Greek word *graphein*, meaning to ‘write’ or to ‘draw’. It is known to be the most thermally stable form of carbon in standard conditions. Graphite can be classified into both natural and synthetic categories. Various graphites within the same classification vary considerably in crystallinity; hence, natural graphite is further sub-divided into flake (crystalline), vein (lump) and microcrystalline (amorphous) graphite. These different types of

natural graphite are each constituted from different ores [1], but flake graphite is the form commonly found in nature.

This naturally occurring crystalline flake graphite occurs as isolated, flat plate-like particles with hexagonal edges if unbroken; when broken, the edges can be irregular or angular. They are generally classified by flake size with diameters ranging from 50 to 800 μm and thicknesses from 1 to 150 μm . Crystalline flakes are obtainable in metamorphosed coal beds and silica-rich quartzites. Due to the high degree of crystalline perfection of their structure, their density, electrical conductivity and thermal conductivity values are close to the theoretical maximum. Flake graphite exhibits excellent compacting properties and has a high carbon content of 90–95% [2]. Furthermore, it can be purified by hydrofluoric and hydrochloric acid treatment, following extraction using similar or the same solvents. The final stage of purification is heat treatment to 1 500 $^{\circ}\text{C}$ under vacuum or, alternatively, by flowing chlorine at 3 000 $^{\circ}\text{C}$ [3].

Vein graphite, also known as lump graphite, occurs in filling fissures (cracks in rocks), and in veins in metamorphic or igneous (formed from molten magma or lava) rocks. This form of graphite has various forms and dimensions from fine powder to lumps of 10 cm in size. The structure is highly crystalline, which provides the material with excellent electrical conductivity. Vein graphite has the highest degree of cohesiveness of all natural graphites [4].

Microcrystalline graphite (commercially called amorphous graphite) is also a coal or soot with no defined crystal structure. It occurs in metamorphic anthracite coal beds or in carbonaceous sedimentary rocks in the form of extremely fine crystalline grains. Its graphite content ranges from 25 to 85%, depending on geological conditions. However, it is a form of natural graphite with a high degree of graphitisation and micro-crystals oriented in different directions.

The high degree of graphitisation of amorphous graphite led to the accidental discovery of synthetic graphite by Edward Goodrich Acheson [5]. He discovered synthetic graphite while manufacturing silicon carbide. Essentially, there are two forms of synthetic graphite, which are produced differently. The first form is electro-graphite, which has a high carbon content and is produced from petroleum coke calcined at 1 300 $^{\circ}\text{C}$. It is then crushed and the blended particles are mixed with binder pitch and extruded to get a green artefact, which is then graphitised at 2 800 $^{\circ}\text{C}$, in an electric furnace [6].

The other form is produced from heating petroleum pitch calcined at 2 800 °C; the resulting synthetic graphite has low density, high porosity and high resistance. However, thermal heating under pressure of materials produced through chemical vapour deposition (CVD) yields synthetic graphite known as highly oriented pyrolytic graphite (HOPG) [7]. Synthetic graphites are polycrystalline materials with variable degrees of crystallite perfection, crystallite dimensions and preferred orientation. They also vary with regard to properties such as electrical resistivity, porosity and optical texture [8]. Graphite products can be moulded into diverse shapes and sizes based on their application.

Interestingly, over the years graphite composites have attracted considerable attention because they can be moulded into various shapes and sizes while their properties are enhanced [7]. Different types of graphite composite have been investigated, including composites from two graphite types. The type of composite first developed by Schulze *et al.* in 1981 [9] consisted of 64 wt% of natural graphite mixed with 16 wt% of synthetic graphite, bound by 20 wt% of phenolic resin; it is referred to as HTR-10. Zhao *et al.* [10] manufactured and characterised spherical fuel elements of HTR-10 composite and concluded that the composite met the requirements of encapsulating tri-structural isotropic (TRISO) fuel. This conclusion was based on the fact that it maintains its structural integrity and strength after irradiation.

1.2 GRAPHITE APPLICATIONS IN NUCLEAR REACTORS

Graphite applications in the nuclear industry were initially discovered with the building of the first self-sustaining chain-reaction reactor in 1942. This discovery led to the use of graphite in reactors, including the South African helium-cooled Pebble Bed Modular Reactor (PBMR) established in 1999 which unfortunately collapsed officially in 2010. In the PBMR nuclear-grade graphite composite HTR-10 is used to encapsulate the fuel kernels, as shown in Figure 1.2. This composite was chosen based on its German design and previous similar successful applications in China's high-technology programme in 2000 [10] and for its ability to maintain its structure after irradiation.

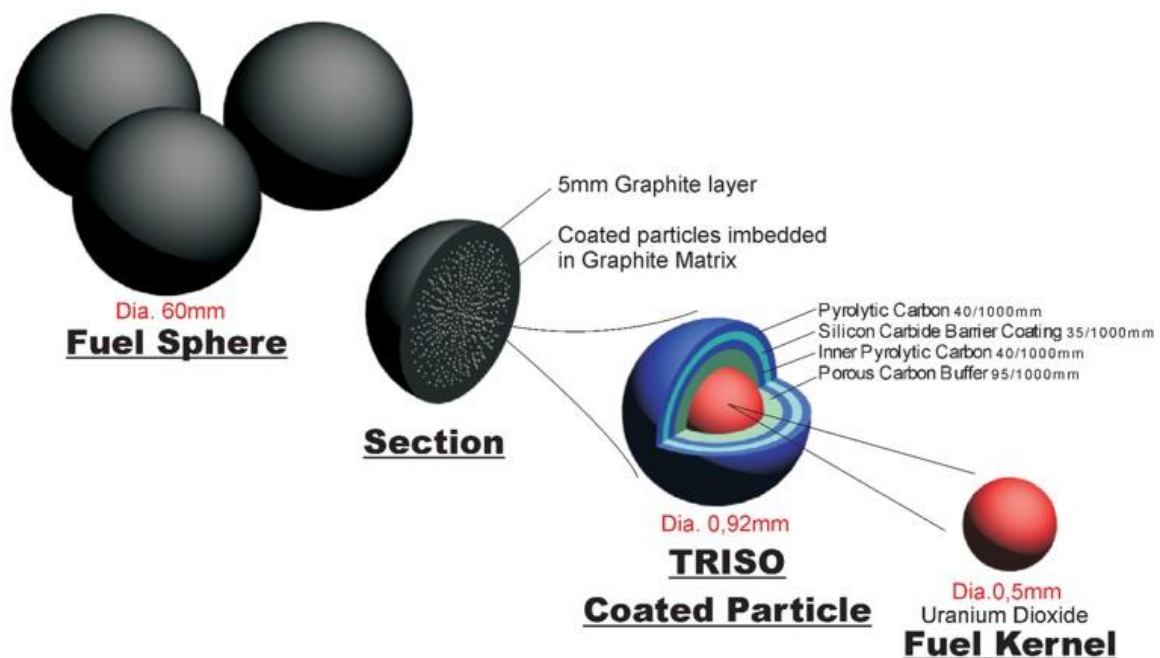


Figure 1.2: The coating layers of fuel kernels into fuel spheres (pebbles).

However, the thermal properties of this composite at low temperature have not been studied. Low-temperature studies are essential in that they give fundamental information about the material. At low temperatures phonons are immobile, but at higher temperatures they asperse the intrinsic properties of the material. At higher temperatures it becomes complex to obtain certain information due to the different processes that occur, such as scattering.

1.3 AIMS AND OBJECTIVES

Since literature on thermal properties of the graphite composite at low temperature is scarce. The aim of this research was to close that gap by studying both the microstructure and thermal properties of pristine and proton-irradiated composite samples at low temperatures.

To achieve the aim as mentioned above, we had to make composite graphite that has properties similar to that of nuclear graded graphite. The reason behind being the applications of nuclear graded graphite in vast fields, more so in nuclear industry. Moreover, considering that South Africa is seriously considering a turn into nuclear energy.

Furthermore, to achieve our objectives we choose a suite of techniques both structurally and thermally to characterize the material. For structural characterization we opted to characterize the material using Raman spectroscopy and X-ray diffraction techniques. Combination of the two methods was understood to be able to give us an understanding of the structural morphology of the material. However, for thermal properties we opted for the Physical Property Measuring System (PPMS) since it had ability to simultaneously to measure thermal conductivity, electrical resistivity and thermo-power. It was through these various technique that were used we where able to conclude the aim and meet the objectives of the study.

Chapter 2 contains the literature review. Chapter 3 outlines the experimental procedures employed to achieve the objectives of the work. The results obtained, which are anomalous to what is expected in irradiated graphite, are discussed systematically in Chapter 4, while Chapter 5 presents the conclusions.

References

1. Boucher, M.B. and Marsh, J.H. (Editors). (1985), *Historica Foundation*.
2. Shibata, T. (2008). *Nucl. Mater.*, **381**: 165–170.
3. Ragan, S. and Marsh, J.H. (1983). *Mater. Sci.*, **18**: 3161–3176.
4. Kelly, B.T. (1981). *Physics of Graphite*. New Jersey: Applied Science Publishers.
5. Tamashausky, A.V. (2006). *Asbury Carbons*, pp. 1–12.
6. Rand, B. and Delhaes, P. (Editors). (1985).
7. Cunningham, N., Lefevre, M., Dodelet, J.-P., Thomas, Y. and Pelletier, S. (2005). *Carbon*, **43**: 3054–3066.
8. Schulze, R.E., Schulze, H.A., Rind, W. and Juelich, G.M. (Editors). (1981), Germany.
9. Zhang, J., Zou, Y. and Tang, C. (2006). *Nucl. Eng. Des.*, **236**: 643–647.
10. Tang, C., Ziqiang, L., Yanwen, Z. and Xiaoming, F. (2008). *Nucl. Eng. Des.*, **238**: 2886–2892.

CHAPTER 2: LITERATURE REVIEW

2.1. GRAPHITE

2.1.1 CRYSTAL STRUCTURE

Carbon atoms in graphite crystal structure have a sp^2 hybridised atomic arrangement. In the sp^2 hybridisation, the s-orbitals combine with two p-orbitals in the L-shell to form three sp^2 hybridised orbitals. The three orbitals are arranged in a planar, trigonal manner with an angle of 120° between them, as shown in Figure 2.1. Furthermore, graphite has a space group of $P6_3/mmc$ [1] and D_{6h}^4 symmetry. The remaining pi bond electrons are delocalised below and above the graphene planes. These are capable of forming weaker bonds with adjacent carbon atoms. This results in weak van der Waals forces between the layers. In the in-plane sp^2 hybrid, the carbon atoms form a planar hexagonal structure.

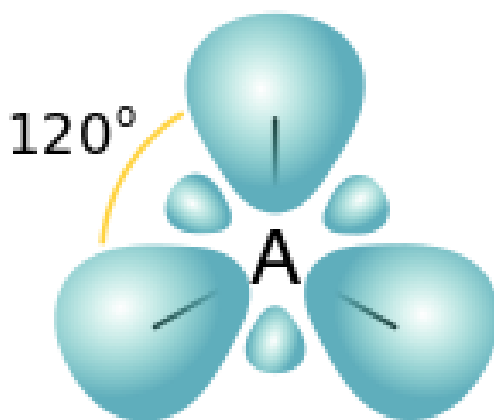


Figure 2.1: Trigonal planar arrangement of sp^2 hybrid

2.1.2 PHYSICAL STRUCTURE

The physical structure of graphite is an infinite stack of hexagonal sheets of graphene. These parallel layers have a spacing between the layers of 3.354 \AA and the in-plane unit cell distance is 2.46 \AA , as illustrated in Figure 2.2. The inter-atomic distance is 1.42 \AA for the carbon-carbon bonds in the basal plane [2].

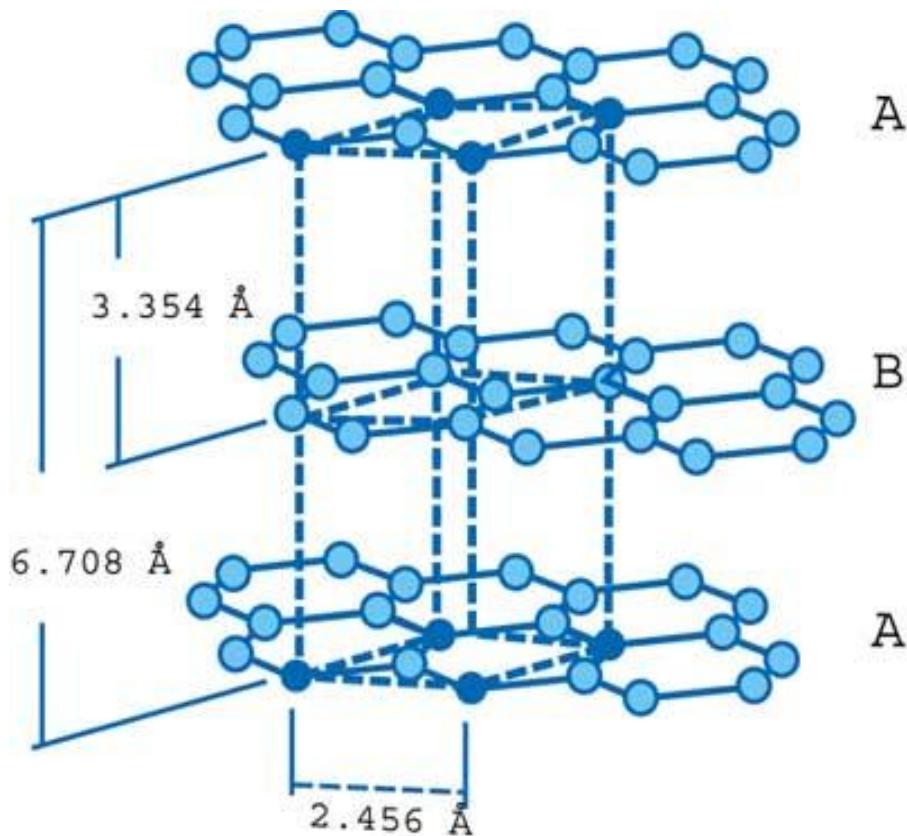


Figure 2.2: Hexagonal graphene layers of bulk graphite

Graphite exhibits both a rhombohedral and a hexagonal crystal stacking structure, as shown in Figure 2.3. The stacking sequence of the hexagonal crystal structure (-ABAB-) repeats with the second layer and is known to be thermodynamically stable and predominantly found in synthetic graphite. On the other hand, the rhombohedral arrangement is such that the first and the third layers counterbalance each other, resulting in -ABCABC- stacking.

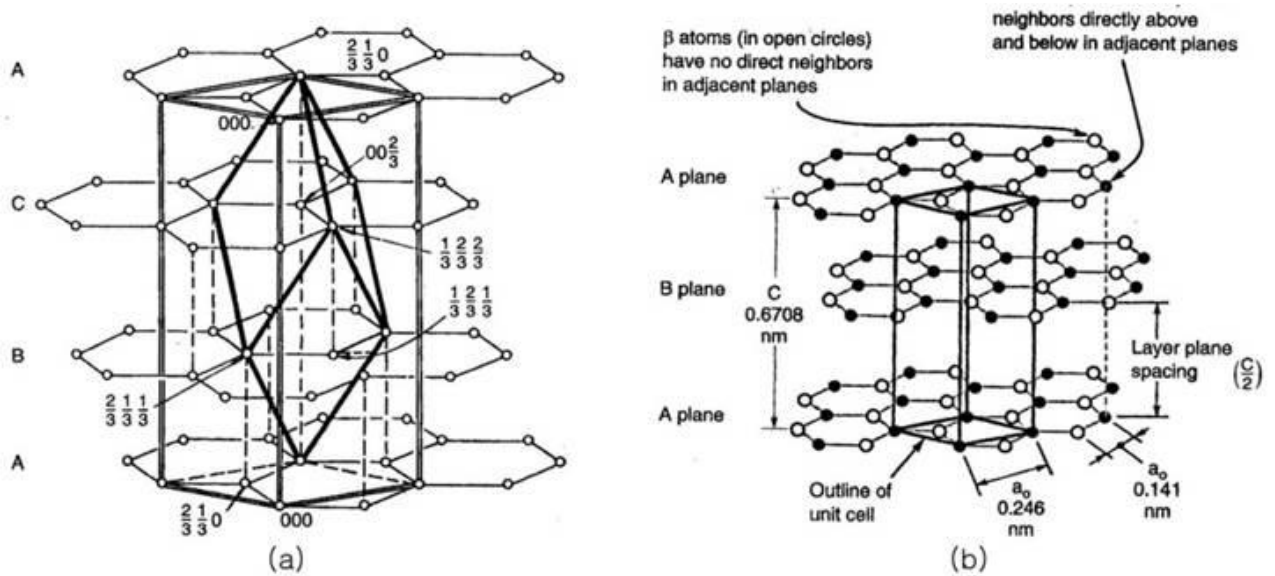


Figure 2.3: (a) Rhombohedral and (b) hexagonal crystal structure of graphite showing the stacking arrangement of the layers.

Natural graphite contains both structures. Each stacking form has a distinct influence on the resulting properties of the graphite specimen. Since rhombohedral stacking is not thermodynamically stable, it can revert to hexagonal stacking with heat treatment to temperatures above 1600 °C [3]. For this reason natural graphite is purified to higher temperatures before its applications and its use in the production of composites. Graphite composites have recently become of great interest due to their potential in technological applications. The different applications of graphite composites are discussed in Section 2.1.3.

2.1.3 GRAPHITE COMPOSITES

Graphite is a well-known carbon allotrope that has diverse applications in a broad range of industries. These applications vary from the production of refractory materials to the production of carbon-based seals for mechanical applications. It is the properties of graphite, such as its high-temperature stability and chemical inertness that have made it so successful in its wide range of applications. This has led to scientists exploring various ways of enhancing existing graphite properties by the production of different graphite composites. Graphite composites can be tailored for a particular application of interest [4].

Carbon-carbon composites or composites reinforced by other materials can be used to enhance the properties of the resulting composite material. Graphite composite (matrix) materials reinforced with fibres and polymers are known to be applicable in the nuclear industry, including as plasma-facing materials [5]. The composite is used because it has enhanced properties, such as better crack resistance and fatigue strength, among other properties [6]. Mixing graphite composite with cement also improves properties such as fracture toughness and plastic behaviour [7]. Hirasawa *et al.* investigated improving the life of lithium-ion batteries through the use of graphite composite [8], while Park and research associates explored safety-related standards of graphite composite applications in these batteries [9].

Over the years graphite has been used as a moderator and the interest has shifted to graphite composites. There are various ways of making graphite composites, including mixing two graphite types. The one that came to be of great interest was what Schulze *et al.* proposed which was graphite composition of 64 wt% of natural graphite and 16 wt% of synthetic graphite, mixed with 20 wt% of phenolic resin as organic binder [10], which is referred to as HTR-10 [11]. Graphite properties are known to be anisotropic [12] and thus they vary with crystallographic direction. In applications as an effective moderator, graphite should be isotropic and thus not change with direction. The HTR-10 composition was developed to compensate the anisotropic properties behaviour of graphite [13]. This behaviour is also attributed to the method of preparation of graphite. Different methods of processing or preparation, either from natural sources or by a synthetic process, lead to the properties being either anisotropic or isotropic. Anisotropic properties are influenced by extrusion and moulding processes during fabrication, while hot pressing prior to graphitisation is used to

achieve isotropic properties for graphite [14]. To ascertain the sustainability of HTR-10 in nuclear applications, further studies were done by various authors. These included work by Tang and associates who explored the composite in the irradiation medium to see whether it would maintain its structural integrity and whether the design would meet the requirements of a 10 MW high-temperature, gas-cooled reactor in China [15]. The properties of the HTR-10 composite were evaluated by Zhao and his colleagues. They concluded that HTR-10 showed no apparent linear dimensional, geometry and strength changes [14].

Nuclear applications expose graphite material to harsh conditions with calamitous effects on the structure and properties of the material. A number of researchers have tried to model what actually happens in that situation. Section 2.2 discusses the process of irradiation and the effects thereof.

2.2 IRRADIATION OF SOLIDS

Irradiation of solids occurs when high-energy particles moving at high speed bombard the surface of the solid. This has recently been widely considered since porous carbon has gained reasonable attention in heat pump applications. Different particles are used for irradiation, such as, neutrons, protons, gamma and alpha particles, etc. When a solid surface is bombarded by high-energy particles, energy is transferred to the solid material in various ways including electrons excitation, due to collision of incident particles which ionize the target atoms. Depending on the energy of the ions, collisions with atoms do occur, in which an atom will be displaced. This process is referred to as ‘primary knock-on atom’ [15]. Moreover, displaced atoms may cause a cascade effect by further displacing other atoms if the energy accumulated initially is high enough. Primary knock-on generally results in a significant portion of the solid being ionised, hence losing its energy.

Nuclear graphite materials can be exposed to such conditions in the nuclear reactor medium where they used as moderators. In this situation their properties are altered by the different defects that are formed due to the radiation exposure. Other exposure conditions, such as the temperature of the medium, play a vital role in defect formation within the material. Graphite materials exposed to high temperature environments undergo an annealing process at temperatures lower than 1 000 °C depending on defects. When annealing takes place, the defected structure may revert to a structure close to that of the original structure. Annealing at room temperature results in close interstitial-vacancy reintegration [15]. This annealing process affects the subsequent properties of the irradiated sample in that some may measure close to the original value before irradiation. Furthermore, energy can be stored within the defects. This is known as ‘Wigner energy’ and influences the annealing process. Although the annealing process may occur, defects within the material are still available and this alters certain properties such as thermal conductivity. Annealing does not always occur either, but takes place mostly in highly damaged graphite at an irradiation temperature of 200 °C. Various defects in graphite [16] have received considerable attention attempted to model the different defects that occur during irradiation. Furthermore there is not much difference between the defects created by charged particles and fast neutrons, except with regard to the distribution of defects [17]. Charged particles tend to lose energy by electronic excitation,

while neutrons penetrate deeper into the material [2]. In the next section the defects that may occur after irradiation are discussed.

2.2.2 RADIATION DEFECTS IN GRAPHITE

2.2.2.1 Interstitial Defects (Point Defects)

Ewels *et al.* [18] computationally studied several interstitial geometries that may be obtained in graphite. The interstitial sites, spiro (bonded to four carbon atoms in each sheet), Y-lid (two bonds to one sheet) and grafted (bonded to two carbon atoms in the same sheet) have the same energy levels in a perfect ABA stacked graphite. The cross-linked (Y-lid and spiro) interstitials are more stable forms of interstitial positions. When an interstitial approaches the V_{β} (vacant lattice site with a ring centre above and below) or V_{α} vacancy, the result can be either an interstitial-vacancy combination (Frenkel-pair defect) or a Stone-Wales (SW) defect (replacement of four hexagons in a graphite sheet by two pentagons and two heptagons when the c-c bond rotates through 90°).

The grafted interstitial can form a graphite structure if it bonds spontaneously with other carbons around the vacancy. However, before that occurs, it may go through sites that can relax into SW defects. It is still uncertain whether this is a way in which SW defects are formed or whether it can relapse back to graphite form. The recombination of interstitial sites with vacancies is exothermic, hence the Wigner energy (internally stored energy). Wigner energy occurs during radiation at temperatures below 250°C [16]. It has been proposed that aggregation of cross-linking defects during radiation may result in changes in the bonding hybridisation of graphite from sp^2 to sp^3 [19].

The defects known as sub-threshold defects occur due to defects, impurities within the material and by creation with lower formation energy than Frenkel-pair defects. Frenkel pairs are estimated to have a total energy of approximately 10 eV which is retained within the crystal as stored energy [20]. An example of low formation energy is the SW defect [21]. This defect was previously considered as a saddle point [22] and later as a mechanism of structural rearrangement in different carbon allotropes such as fullerenes [23].

2.2.2.2 Interstitial Clusters

The homogeneous nucleation process, in which interstitial defects are mobile, was first proposed by Reynolds and colleagues [24, 25]. When the defects migrate from one area to another, they eventually assemble and by so doing they reduce their energy in order to form less mobile defect regions referred to as ‘clusters’. However, di-interstitials have been observed to be responsible for various property changes in radiated graphite. Iwata *et al.* [26] put forward the theory of the presence of multiple carbon dimers in bulk graphite, abbreviated as $(I)_n$. This defect has been proposed to occur in temperature region of 80–120 K.

2.2.2.3 Vacancy Defects

During irradiation depending on the energy of incident particles some atoms get displaced from their original positions to interstitial positions leaving what is known as ‘vacancies’, as indicated in Figure 2.4. Due to the rearrangement of atoms after radiation, these vacancies are able to migrate within the lattice at a slower rate compared with interstitial defects [27] this causes what is known as contraction and expansion of the plane. Single vacancies are said to exist in significant concentrations due to their lower rate of aggregation and absorption at the boundaries. Larger vacancies begin to form at higher temperatures of more than 920 K [28]. Defects of this type are accompanied by interstitial defects.

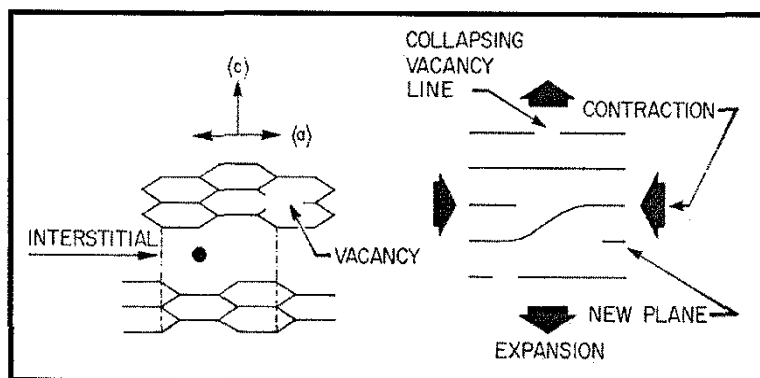


Figure 2.4: Interstitial and vacancy defects simulated in a graphite layer

2.2.2.4 Buckling and Folding Defects

Interstitial defects within graphite may induce other defects. These have been explored using Density Functional Theory (DFT) [21]. The aim was to try to understand how these defects occur. The study of irradiated graphite using high-resolution electron microscopy (HREM) has revealed the breaking and bending of sheets [29].

It is anticipated that a layered material will undergo buckling and folding of layers depending on the integrity of the layers after irradiation. This type of defect (buckling) results from a sheet linked at two places (spiro or Y-lid point defects) with one bond longer than the other. Buckling is caused by irradiation of graphite at temperatures lower than 250 °C and when dislocations of opposite signs interact with each other on different glide planes [6].

Ewels *et al.* did calculations based on first principles to confirm buckling at the circumference where the core of non-basal edge dislocations gives rise to interlayer bonds [6, 18, 30]. At higher temperatures the damage in graphite involves folding of the layers, leading to what is referred to as ‘ruck and tuck’ defects. Ruck defect atoms originate from the basal dislodgment glide and not from the Frenkel pairs or the point defects [30].

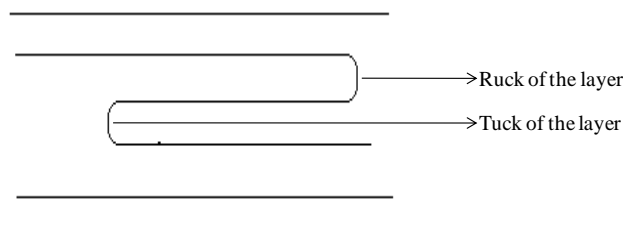


Figure 2.5: Schematic diagram of the ruck and tuck as shown drawn by Heggie *et al* [16].

These defects models try to explain what occurs after irradiation. Previously researchers have concentrated on structural defects and the structural properties that are affected by irradiation defects. However, irradiation of graphite has effects on its physical properties, such as structural and thermal properties, just to mention a few.

2.2.3 EFFECTS OF RADIATION ON GRAPHITE

2.2.3.1 Structural Effects

The different types of defect described in the previous sections harden the material; hence the material obeys Hooke's law. Depending on the irradiation dose as well as the ions used, graphite undergoes dimensional changes. The expansion along the c-direction (perpendicular to the alignment of the layers) is known as the 'creep effect' [30]. This usually occurs at temperatures below 350 °C. The expansion is due to the weak van de Waals forces along the c-direction. The shrinkage along the a-direction (basal plane) is due to the formation of interstitials, interstitial clusters, vacancies and collapsed vacancy lines [30, 31]. The creep effect induces stress and strain within the material, which also contributes to further decay of the material properties [31]. In addition to the creep effect, irradiation causes rhombohedral stacking faults to revert back to hexagonal stacking faults at higher temperatures [2]. Furthermore, in a higher temperature range (400–1400°C) graphite is known to undergo what is known as 'radiation-induced contraction', which results in decrease of strength and elastic modulus. At higher temperatures in the reactor medium the material may go through an annealing process (the deformed structure is stabilised). When this happens, the material properties that have changed during irradiation return fully or approximately to the original values [32]. Structural alteration affects not only the physical properties, but also the thermal properties of graphite material.

2.2.3.2 Thermal Effects

Thermal conductivity (K)

Thermal properties are of the utmost importance in nuclear applications, especially thermal conductivity, which is the ability of a material to conduct heat. The electronic contribution to the total thermal conductivity can be calculated from the so-called Wiedeman-Franz law shown in equation 2.1 below [2]:

$$K_e = (T/L)\rho \quad (2.1)$$

where L is the Lorentz constant (2.8×10^{-8}), T is the temperature and ρ is the electrical resistivity. The dominance of electrons in conductivity at low temperatures of less than 2 K decreases as the temperature increases due to various scattering processes. At higher

temperatures phonon-phonon, electron-electron, phonon-electron, electron-grain boundary scattering processes occur which decrease the electron contribution [28]. Electrons do not affect the mean free path (distance travelled by a particle before it is scattered) of phonons [33]. The mean free path can be computed through the application of the Equation 2.2:

$$l = 3K/vC_T \quad (2.2)$$

where K is thermal conductivity, C_T is the total heat capacity and v is the mean velocity.

The thermal conductivity of graphite is dependent on various structural aspects of the material, such as crystallite size, non-graphitic regions within the material, porosity, crystalline imperfections and orientation of the crystallites [34]. The low-temperature dependence of thermal conductivity was well explored decades ago and available data is insufficient on composite graphites. For highly oriented graphite the low temperature dependence is said to be T^2 [35]. However, authors have considered different graphite grades and the temperature dependence obtained varied from T^2 to $T^{2.3}$ [36]. This temperature dependence gives information about the crystal perfection of the material. Hence, this anomalous temperature dependence is attributed to the presence of non-graphitic regions (binders such as un-graphitized coke or pitch residue). However, if at very low temperatures electronic transport is dominant, a linear temperature dependence is expected [37].

Graphite is known to have the high thermal conductivity as compared to most non-metallic materials at ambient temperature. After irradiation exposure, thermal conductivity is known to decrease significantly due to the irradiation induced defects. Previous work has shown that after neutron irradiation, conductivity may decrease by up to one-tenth of its original value [38]. This is attributed not only to the defects induced, but also to the scattering processes, including defect scattering [39], that occur.

Seebeck coefficient (thermo-power)

The Seebeck effect refers to the migration of charge carriers from hot foot to cold foot within the material, which results in a variation of voltage between the two points. There are two carriers that contribute to the Seebeck coefficient ($S(T)$), namely negative carriers and positive carriers [37]. Over the years data have been reported on the thermo-power of graphite since the initial attempt to study the Seebeck coefficient of graphite by Tyler and Wilson [34]. Graphite is known to exhibit a minimum $S(T)$ at 35 K; which has been associated with phonon drag [37]. Phonon drag is an increase in the effective mass of conduction electrons or valence holes, as a result of interactions with the phonons in which the electrons are dissipated. This $S(T)$ is also sensitive to structural imperfections and thus a deeper minimum reflects structural imperfections. However, when a magnetic field is introduced, there is a significant change in the valence hole and electron dominance of thermoelectric power, namely an increase to the positive region [37] which reflects the dominance of the holes.

REFERENCES

1. Regan, S. and H. Marsh, *J. Mat. Sci.*, (1983). **18**: p. 3161-3176.
2. Reynolds, W.N., ed. P.E. Evans and L. Holliday(1968), Amsterdam: Elsevier.
3. Parthasarathy, G., B. Sreedhar, and T.R.K. Chetty, *Current Sci.*, (2006). **90**: p. 995-1000.
4. Xiao, P., M. Xiao, and K. Gong, *J Poly.*, (2001). **42**: p. 4813-4816.
5. Wu, C.H., J.P. Bonal, and B. Thiele, *J. Nucl. Mater.*, (1994). **212**: p. 1168-1173.
6. Blackstone, R., *J. Nucl. Mater.*, (1977). **65**: p. 72-78.
7. Wen, S. and D.D.L. Chung, *Carbon*, (2002). **40**: p. 2495-2505.
8. Hirasawa, K.A., et al., *Power Source*, (1997). **69**: p. 97-102.
9. Park, Y.S. and S.M. Lee, *Electrochim. Acta*, (2009). **54**: p. 3339-3343.
10. Cunningham, N., et al., *Carbon*, (2005). **43**: p. 3054-3066.
11. Schulze, R.E., et al., (1981): Germany.
12. Slack, G.A., *Phys.Rev. B*, (1962). **127**: p. 694-701.
13. Tang, C., et al., *J.Nucl. Eng. Des.*, (2008). **238**: p. 2886-2892.
14. Zhao, H., T.X. Liang, and J. Zhang, *J.Nucl. Eng. Des.*, (2006). **236**: p. 643-647.
15. Nightingale, R.E., (1962), London: Academic Press.
16. Heggie, M.I., et al., *J. Nucl. Mater.*, (2011). **413**: p. 150-155.
17. Telling, R.H., et al., *Nature. Mater.*, 2003. **2**: p. 333-337.
18. Ewels, C.P., et al., *Phys. Rev. Lett.*, (2003). **91**: p. 025505.
19. Tanabe, T., *Physica. Scripta*, (1996). **T64**: p. 7-16.
20. Simmons, J.H.W., ed. J.V. Dunworth. Vol. 102. (1965), London: Pergamon Press.
21. Telling, R.H. and M.I. Heggie, *Philos. Mag. Lett.*, (2003). **83**: p. 411-421.
22. Dienes, G.J., *J. Appl. Phys.*, (1952). **23**: p. 1194-1199.
23. Stone, A.J. and D.J. Wales, *J. Chem. Phys. Lett.*, (1986). **128**: p. 501-509.
24. Reynolds, W.N. and P.A. Thrower, *J. Philos. Mag.*, (1965). **12**: p. 573-582.
25. Lidiard, A.B. and R. Perrin, *J. Philos. Mag.*, (1996). **14**: p. 433-437.
26. Iwata, T., *J Nucl. Mater.*, (1985). **133**: p. 361-364.
27. Thrower, P.A., *J. Chem. Phys.*, (1969). **5**: p. 217-220.
28. Tanabe, T., et al., *Fussion Eng. Des* (1995). **29**: p. 428-434.
29. Spalaris, C.N., L.P. Bupp, and E.C. Gilbert, *J. Phys. Chem.*, (1957). **61**: p. 350-354.
30. Burchell, T.D. and L.L. Snead, *J. Nucl. Mater.*, (2007). **371**: p. 18-27.
31. Wang, H. and S. Yu, *J.Nucl. Eng. Des.*, (2008). **238**: p. 2256-2260.

32. Matsuo, H. and T. Honda, J Nucl. Mater., (1972). **45**: p. 79-81.
33. Snead, L.L., J Nucl. Mater., (2008). **381**: p. 76-82.
34. Tyler, W.W. and A.C. Wilson, Phys. Rev., (1952). **89**: p. 870-875.
35. Hove, J.E. and A.W. Smith, Phys. Rev. B, (1956). **104**: p. 892-900.
36. Klein, C.A. and M.G. Holland, Phys. Rev., 1964. **136**.
37. Ayache, C. and A.D. Combarieu, Phys. Rev. B, (1980). **21**: p. 2462-2465.

CHAPTER 3: EXPERIMENTAL

3.1 MATERIALS

The material used for this study is a composite graphite which consists of 64 wt% of natural graphite (NG: GrafTech: GPN-B-G1) and 16 wt% of synthetic graphite (SG: PBMR: SGL-94941/1-1), bound together with 20 wt% of phenolic resin (PBMR: Novolak-type).

3.2 COMPOSITE PREPARATION METHOD

Graphite composite powder was prepared by mixing 64 wt% of natural graphite with 16 wt% of synthetic graphite for approximately 1 h in a z-blade mixer (Jones mixers). 20 wt% of phenolic resin was prepared by dissolving resin crystals in excess methanol (Sigma Aldrich: 99%). The resin mixture was then mixed with the graphite composite powder to form a graphite composite paste. The paste was dried for 6 h at 70 °C and milled using a carbon steel ring mill (at room temperature, for 10 min). The milled composite was sieved at a range of 0–212 µm using electromagnetic shakers. The resulting 120 g of graphite powder composite was uni-axially pressed (Vertex Automation Pty (Ltd)) at pressure levels of 10 and 19.5 MPa for 1 h in a stainless steel disc mould (prepared at the University of Pretoria) as detailed by P Magampa *et al* [1]. The pressed mould had the following dimensions: height of 10 mm, outer diameter 120 mm and inner diameter 100 mm. The moulded sample was cut using a Buehler IsoMet 4000 linear precision saw with carbon blade under dry conditions into the following dimensions: length 100 mm, width of approximately 15 mm and height 10 mm. The cut samples were carbonised at a temperature of 950 °C and heat treated to an annealing temperature of 1 800 °C using a Thermal Technologies (LLC) graphitising unit. Finally, the samples were further cut into smaller dimensions of 2.5 x 2.5 x 10 mm for irradiation experiments, structural characterisation and thermal conductivity measurements.

3.3 CHARACTERISATION TECHNIQUES

3.3.1 STRUCTURAL CHARACTERISATIONS

3.3.1.1 Raman Spectroscopy

Raman spectroscopy was used in this research with the aim of investigating the effect of radiation on the composite with respect to its structural imperfections. Raman spectroscopy data on the graphite composite samples were collected using a T64000 micro-Raman spectrometer from HORIBA Scientific, JobinYvon Technology, equipped with a triple axis monochromator system to eliminate contributions from the Rayleigh line shown in Figure 3.1. All the samples were analysed with a 514 nm argon excitation laser (6 mW to avoid thermal effects) in a back-scattering configuration through an LD X 50 objective Olympus microscope attached to the instrument, with recording times of 120 s and a resolution of 2 cm^{-1} .

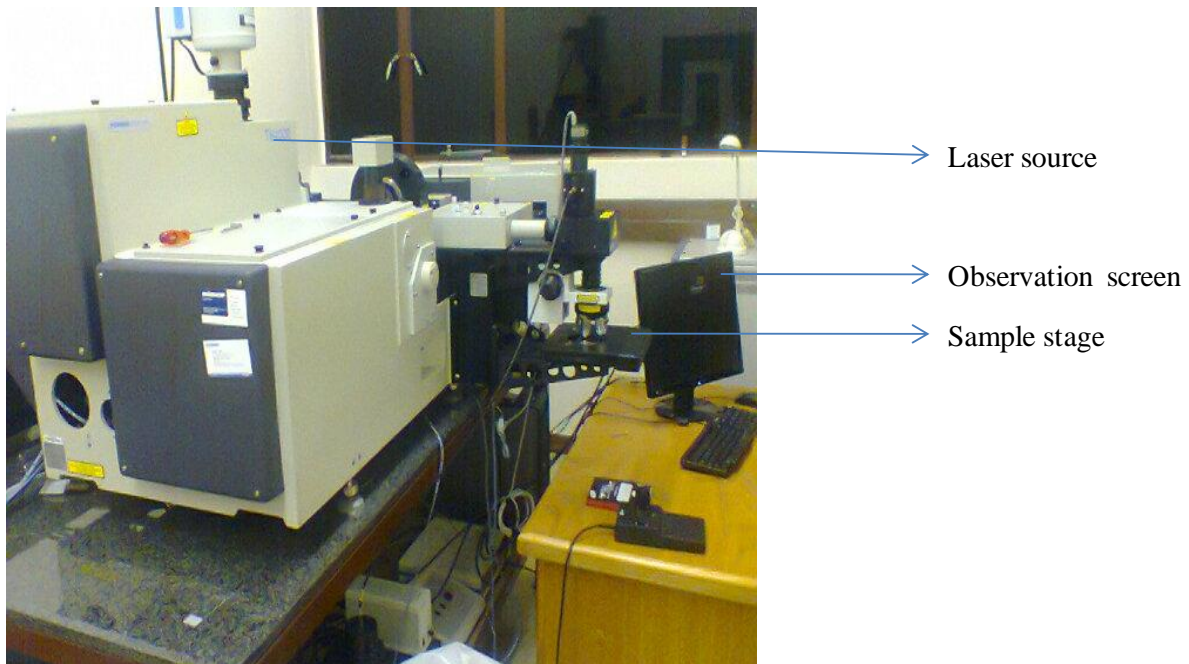


Figure 3.1: Raman spectroscope used for structural characterisation

3.3.1.2 X-Ray Diffraction (XRD)

The diffraction patterns were recorded at room temperature using a Bruker D8 Advanced Power Diffractometer (figure 3.2a) in Bragg-Brentano geometry operated at 40 kV and 40 mA using CuK α radiation. The goniometer set-up (Figure 3.2b) included a Vantec-1 detector with Ni-filter and 2° Soller slit on both incident and diffracted beams, providing narrow and symmetrical instrumental profiles over the required angle range.

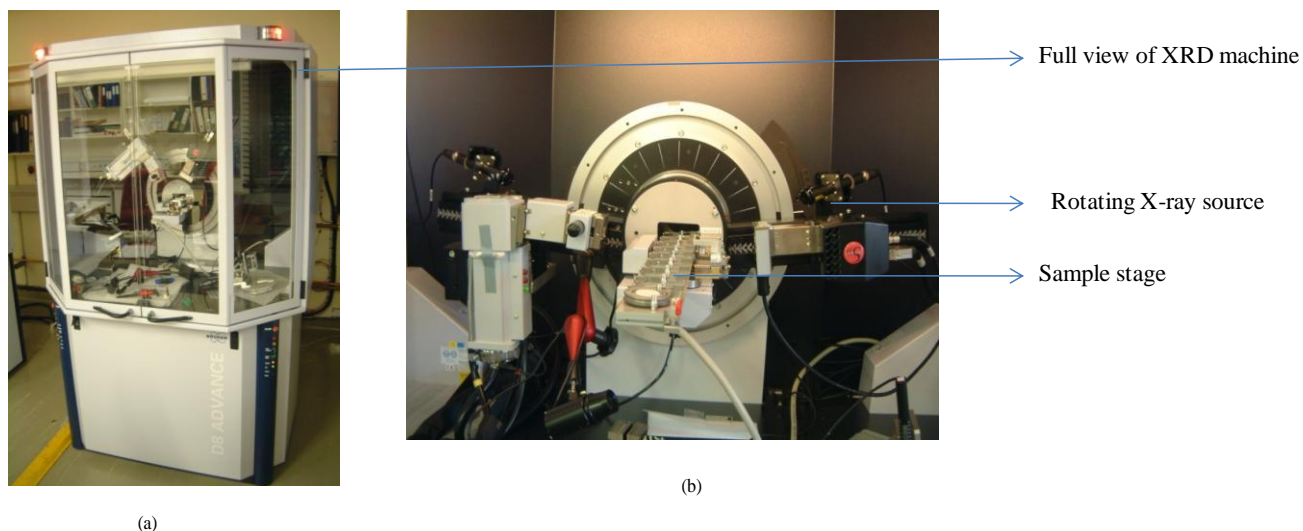


Figure 3.2: The Bruker D8 Advanced XRD machine: (a) full view of the machine, and (b) closer view of the goniometer, the X-ray source, the sample holder/stage and the detector

The XRD patterns of the samples were recorded in the range ($2\theta=15-90^\circ$) using a step size of 0.04° and a counting time of 20 s per step, in each case without moving the solid sample. The instrumental profile was obtained experimentally by collecting the diffraction data of a standard Al_2O_3 (corundum) powder, fitting them with pseudo-Voigt functions and parameterising the trends of the full width at half maximum (FWHM) as well as the shape parameters as functions of 2θ according to the Caglioti expression [2] and a 2θ linear function using the PM2K software. Qualitative phase analysis (search match) was done using the PAN Analytical X'pert High score plus software employing the ICDD 2007 PDF-2 database. The whole powder pattern modelling (WPPM) method [3] implemented in the PM2K software [4] was employed for the micro-structural analysis. In addition to the peak intensities, unit cell

parameters and coefficients of Chebyshev polynomial background, the microstructure parameters refined are the lognormal standard deviation (σ), lognormal mean (μ) and lognormal distribution of cuboidal crystallite domain size.

Preliminary calculations of the interlayer spacing were done using the Bragg equation (3.1), which explains the incoherent and coherent scattering within the material.

$$d = n\lambda / 2 \sin \theta \quad (3.1)$$

where d is the interlayer-spacing, λ is the wavelength and θ is the angle between incident and reflected beam.

3.3.2 THERMAL TRANSPORT MEASUREMENTS

Thermal properties were measured using a Quantum Design Physical Property Measuring System (PPMS) Model P600, as shown in Figure 3.3. The data were collected and analysed using Firmware software. The system can simultaneously measure the thermal conductivity, Seebeck coefficient and electrical resistivity properties of a material, with measurements done in a continuous mode.

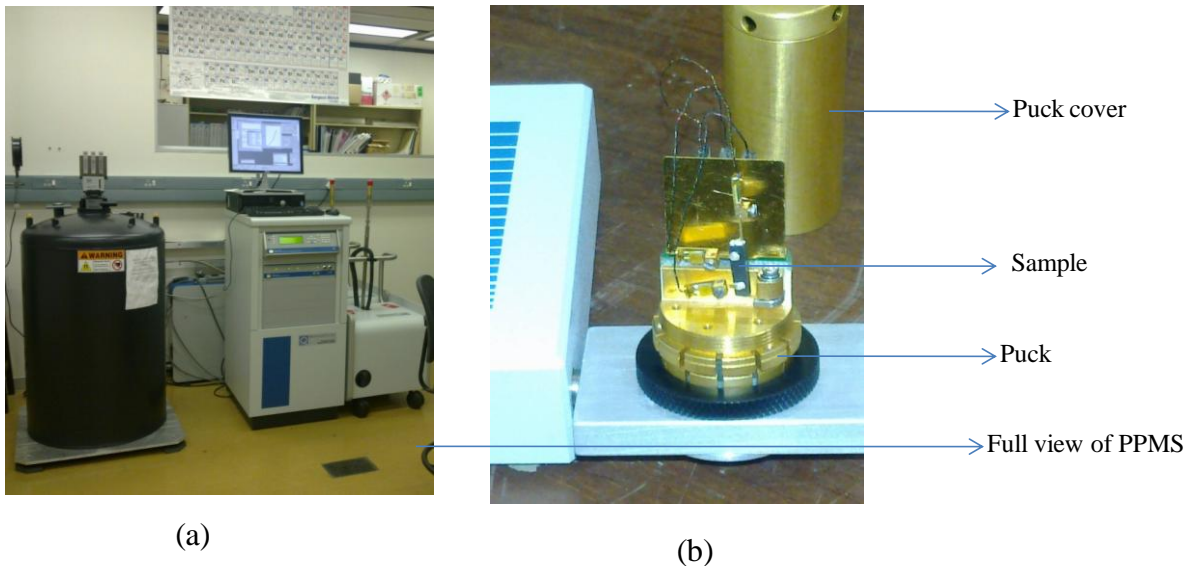


Figure 3.3: The Quantum Design Physical Property Measuring System: (a) showing the overall view of the system and (b) the sample holder (puck)

3.3.2.1 Sample Preparation

Samples were first cleaned by sanding the surface, then leads (copper leads with a gold coating) were attached in a four-probe geometry using (silver-filled epoxy) paste as shown in Figure 3.4. The samples then underwent a curing stage at 120 °C for 2 h to harden the epoxy-attached leads on the sample surface, and thereafter they were loaded into the puck and into the PPMS. [you need

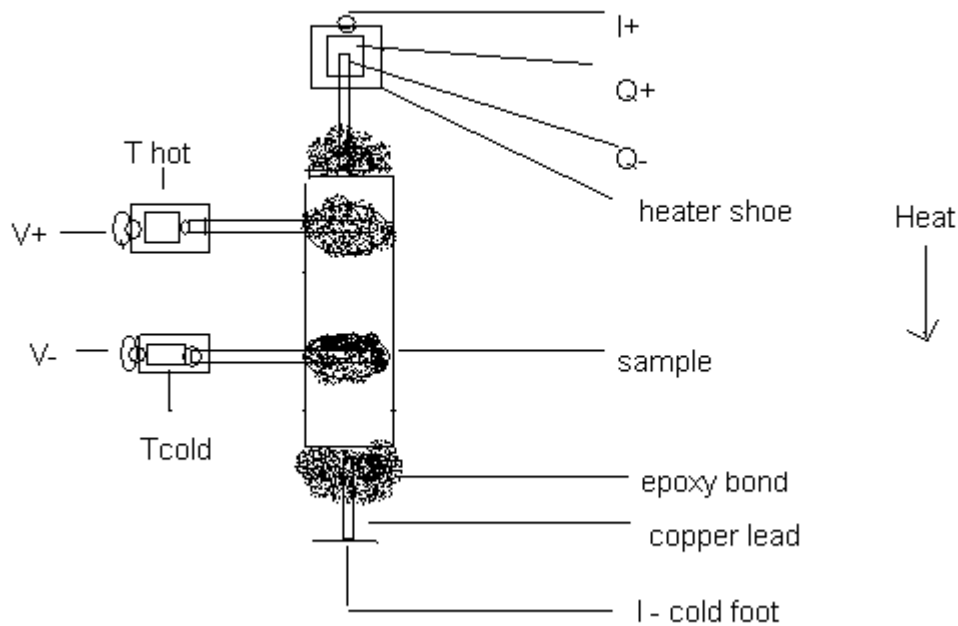


Figure 3.4: Four-probe geometry of thermal and electrical connections.

3.3.2.2 Measurement Process Description

In continuous mode the parameters of heater power and period, including the resistivity excitation and frequency, are continuously updated after each heat pulse to keep the temperature rise and period ratio parameters near the user-set values. This is done by fitting the raw data ΔT (time) in the algorithm (equation 3.4), which performs a three-parameter, non-linear, least-squares fit in asymptotic temperature ΔT_{∞} . The asymptotic temperature drops across the sample, as well as τ_1 and τ_2 , which are long and short time constants

respectively and which characterise the sample-lead-shoe (Combined Circuit) thermal circuit. ΔT is used to calculate the thermal conductivity of the sample.

$$K = (\text{heat power}) / \Delta T_{\infty} \quad (3.4)$$

where K is the thermal conductivity of the material. The period of the next measurement is computed from τ_1 using the following expression (equation 3.5):

$$\text{Period} = (\text{period ratio})(\tau_1) \quad (3.5)$$

The asymptotic Seebeck voltage is computed from raw data ΔV (time) similarly, except that a computationally simple linear regression is used because τ_1 and τ_2 are based on a conductivity fitter routine. The Seebeck coefficient is simply:

$$\alpha = \Delta V_{\infty} / \Delta T_{\infty} \quad (3.6)$$

Resistivity measurements are made before and after the heat pulse and the average of the two is taken as the sample resistivity.

3.3.2.3 Thermal and Electrical Circuit

Both the thermal and electrical connections are shown in Fig. 3.4. For thermal conductivity and Seebeck coefficient measurements, heat is applied to one end of the sample by running current through the heater ($Q_{+/-}$). The temperatures T_{hot} and T_{cold} are measured at the thermometer shoes. During the heat pulse, the Seebeck voltage ($\Delta V = V_{(+)} - V_{(-)}$) is monitored, while the heat exits the sample through a cold foot.

Electrical resistivity measurements are made both before and after the heat pulse as detailed above. The current ($I_{+/-}$) flows through the sample and the voltage drop across the sample is monitored using $V_{+/-}$ leads (see Figure 3.4)

3.3.3 PROTON IRRADIATION

Irradiation was done using Van de Graaff accelerator scanning proton microscopy at iThemba labs (Gauteng), as shown in Figure 3.5. Proton particles were generated from the Source of Negative ions by Cesium Sputtering (SNICS) through a technique known as Proton-Induced X-ray Emission (PIXE) and accelerated to the sample with 2 MeV energy and a current of ~ 2 nA. A lithium-drifted silicon X-ray detector was used, cooled by liquid nitrogen. The data were collected using an Oxford Microbeams Data Acquisition system (OMDAQ 2007). Irradiation was done at room temperature for 3 and 4.5 h respectively, which corresponds to fluences of 2.2×10^{12} and 2.2×10^{14} protons/cm² respectively.

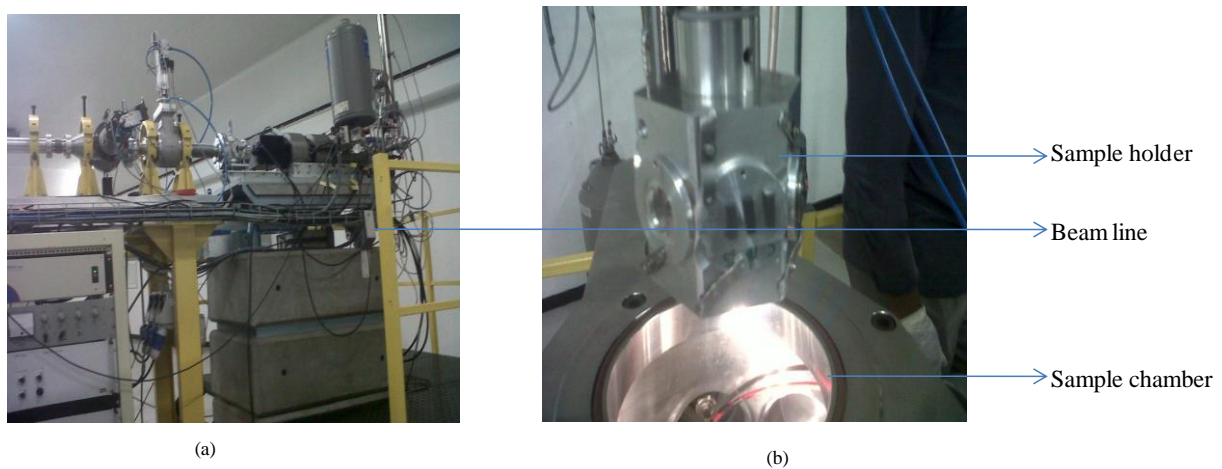


Figure 3.5: Van de Graaff scanning proton microscope used for irradiation of the samples: (a) indicates the part of the beam tube where the beam is channelled to the target and (b) shows the sample holder and the vacuum chamber in which the holder is inserted for measurements.

REFERENCES

1. Magampa, P.P., N. Manyala, and W.W. Focke, *J. Nucl. Mater.*, (2013). **436**: p. 76-83.
2. Caglioti, G., A. Paoletti, and F.P. Ricci, *Nucl. Instrum. Methods*, (1958). **3**: p. 223-228.
3. Scardi, P. and M. Leoni, *Acta Crystallogr.*, (2002). **A58**: p. 190-200.
4. Leoni, M., T. Confente, and P. Scardi, *Z. Kristallogr.*, (2006). **22**(249).

CHAPTER 4: RESULTS AND DISCUSSION

4.1 STRUCTURAL CHARACTERISATION

The graphite composite was structurally characterised by both Raman spectroscopy and X-ray diffraction for determination of disorder and structure, which helped in the estimation of average crystallite sizes. However, in this section only the findings observed for the high-pressure (19.5 MPa) samples are discussed. High pressured sample have been noted to have less porosity of about 25 % in comparison to 40 % of 10 MPa pressured samples.

4.1.1 RAMAN SPECTROSCOPY

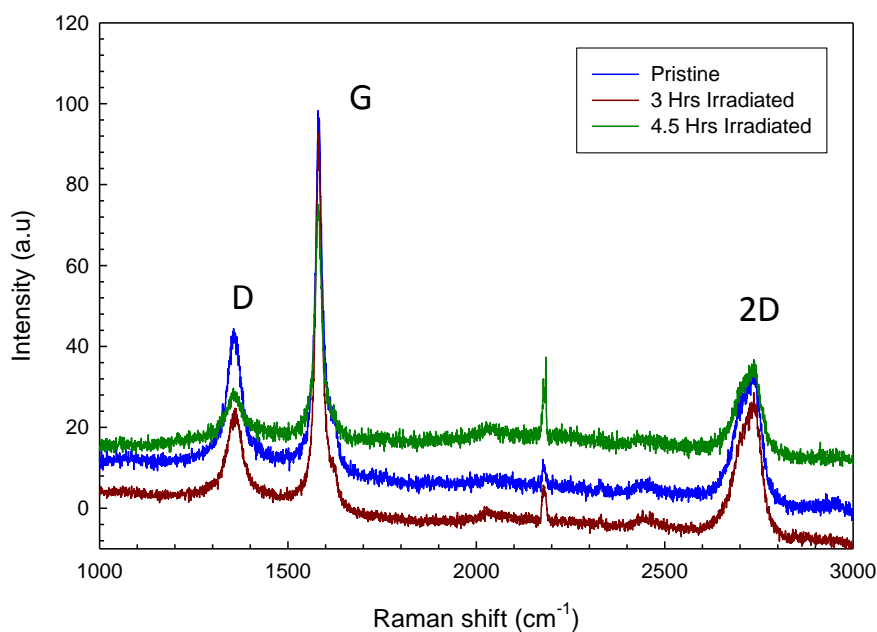


Figure 4.1: Comparison of Raman spectra of pristine and irradiated samples for 3 and 4.5 hrs respectively.

Figure 4.1 shows the Raman spectra of pristine samples and those irradiated for 3 and 4.5 hrs, which show distinct graphite peaks. The D peak is usually attributed to defects sides in the sample which in our case could be mainly coming from non-graphitic binder used during samples synthesis. The comparison of pristine sample to those of 3 and 4.5 h irradiated samples shows much-reduced D-peaks irradiated samples, which is quite surprising since one

would expect more significant disorder which would be attributed to defects induced by proton irradiation within the material. The D-peak is an in-plane A_{1g} zone (edge mode), which is silent for infinite layer dimension but active for imperfect layers. This shows that there is an improvement in the structure of the material due to irradiation. The G-peak is Raman active with an eigen value of E_{2g} , which is attributed to the graphitic nature of the material. Furthermore, the G-peak is due to the stretching of the sp^2 bonds in all pairs of rings and chains. Through Raman spectroscopy it was possible to establish the crystallite improvement of the defected specimen through proton irradiation.

4.1.2 X-RAY DIFFRACTION (XRD) PATTERN

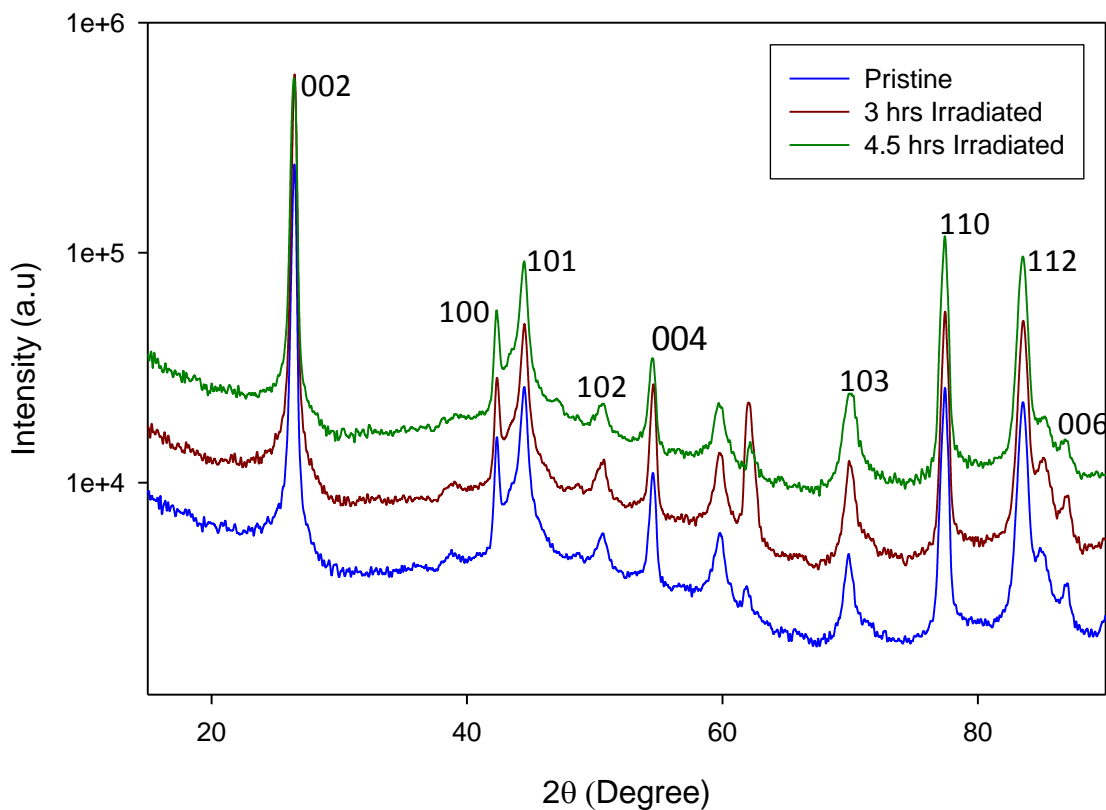


Figure 4.2: X-ray diffraction (XRD) patterns for the graphite composite

Figure 4.2 shows the XRD patterns of the graphite composite, with intensity plotted on a linear scale. The diffraction patterns of all samples are dominated by strong ($00l$) reflections at 26.4° as indicated in the figure. On the other hand, the (101) peak has merged with the rhombohedral phase peaks to form a broad peak which is adjoined with the distinguishable hexagonal phase peak (100). The merging of the rhombohedral phase and the hexagonal phase has contributed to the wedge formed between the (101) and (100) peaks. The (102) peak is attributed to diffraction of the planes in the aligned orientation. There is shift of peaks towards the higher order of 2θ ; this may be attributed to compression stress within the material. Through the patterns Table 4.1.

Table 4.1: Interlayer spacing of both pristine and irradiated samples of the high pressure samples.

Sample	Interlayer spacing (Å)	Crystallite size (Å)	Degree of Graphitization (%)
Pristine	3.3649	330	63
Irradiated for 3 h	3.3985	422	64
Irradiated for 4.5 h	3.3989	480	72

Table 4.1 shows the interlayer spacing of the composite samples. It was observed that as the radiation exposure is increased the interlayer spacing increases. However, between the radiated samples the interlayer spacing increases slightly. This may also suggest that there is an increase in the in the crystallites sizes which accounts for this growth in the spacing. This shows structural improvement of the sample which is in agreement with shown Raman spectroscopy data presented in figure 4.1. However, looking at the crystallite size there is an increase with respect to irradiation exposure. This is further seen in the degree of graphitisation which also improves with irradiation. Degree of graphitization is influenced by various factors including stress and strain, for this composite maybe caused by uni-axial pressing.

4.2 THERMAL CHARACTERISATION

Thermal characterisation was done for the graphite composite using the Physical Property Measuring System (PPMS) which is capable of simultaneous measurements of thermal conductivity, electrical resistivity and Seebeck coefficients on the same sample.

4.2.1 INTRODUCTION

The sample that was used for this study was expected to behave like a graphite specimen since it is a combination of two types of graphite. However, in order to explain the thermal conductivity data obtained, use was made of the approach of Hove and Smith [1]. Their analysis was based on graphite that consisted of two types: one graphitic and the other non-graphitic. In this model the sample used simulates the graphite composite that was used for this study as fully described in Chapter 3. The un-graphitised region is poorly crystalline and has a highly disordered diamond-like structure with tetravalent bonding. Hence interpretation of the data required acceptance of the hypothesis that un-graphitised material exists in sufficient quantities to form three-dimensional isotropic heat conductors in series with the graphitic region in the material. At low temperatures the non-graphitic region conducts heat in an isotropic manner with Debye dispersion. The temperature dependence of the thermal resistivity of the graphitic region is inversely proportional to the temperature dependence of the specific heat of the graphitic region, thus T^2 . Temperature dependence of non-graphitic region has been studied to be T^3 . Since the two regions are taken to be in series, the total temperature dependence of the thermal resistivity will be T^3 at very low temperatures and T^2 at higher temperatures [1]. The total resistivity can be formulated as follows:

$$\frac{1}{k} = \frac{\alpha}{Sk_2} + \frac{(1-\alpha)}{k_3} \quad (4.1)$$

where k_2 and k_3 are the conductivities of the graphitic and non-graphitic regions respectively, α is the volume fraction of the graphitic region and S is the effective graphitic fraction orientated to permit heat flow in the direction of the temperature gradient since the group velocity is given by:

$$v_3 = \left(\mathcal{R}\theta_3/h \right) \left(4\pi V_3/3N_3 \right)^{\frac{1}{3}} \quad (4.2)$$

and

$$v_2 = \left(\mathcal{R}\theta_2/h \right) \left(\pi A_2/N_2 \right)^{\frac{1}{2}} \quad (4.3)$$

where θ_2 is the corresponding Debye temperature and A_2 is a constant.

From equations 4.2 and 4.3 the thermal conductivities can be written as follows:

$$k_3 = \frac{1}{3} C_3 v_3 l_3 \quad (4.4)$$

and

$$k_2 = \frac{1}{2} C_2 v_2 l_2 \quad (4.5)$$

By substituting equations 4.2, 4.3, 4.4 and 4.5 into equation 4.1 and multiplying both sides by T^3 , Smith *et al* showed that equation one reduced to 4.8 which is much practical equation to use to analyse you data:

$$\frac{T^3}{k} = \frac{\alpha T}{S l_2} + \frac{60(1-\alpha)}{l_3} \quad (4.6)$$

where T is the absolute temperature, l_2 is the crystalline length at low temperatures, l_3 is the average distance between graphitic regions or the scattering path of phonons within the non-graphitic region, S is the effective fraction of the graphite which is oriented to permit heat flow and α is the volume fraction of the specimen which is graphite [1].

However, it is assumed that the scattering probability can be adequately described by the linear expression:

$$\frac{1}{l_2} = \frac{1}{L} + aNv \quad (4.7)$$

where L is the average crystallite length, v is the frequency of the scattered wave and N is the volume density of the defects.

This assumption leads to an expression which describes the correct qualitative behaviour regardless of scattering type:

$$\frac{T^3}{k} \cong \left(\frac{\alpha}{5L}\right)T + \left(\frac{\alpha}{5}Ng\right)T^2 + \frac{60(1-\alpha)}{l_3} \quad (4.8)$$

Equation (4.8) is the key equation that was used to analyse our data and from the fit to our experimental data helps to determine crude values of l_3 , which is the parameter to be compared to structural data which helps to understand the behaviour of thermal properties of our samples. However, we have opted to look at the thermal resistivity where we can take the two regions (graphitic and non-graphitic) within the material are in series.

4.2.2 THERMAL CONDUCTIVITY

This section looks at the thermal conductivity of the composite for both the pristine and irradiated samples. The pristine sample will be considered first so as to examine the two normal contributions to thermal conductivity, namely the electron and phonon contributions, in both the parallel and perpendicular directions of the samples in relation to the moulding pressure direction, as described below.

4.2.2.1 Pristine Data

The pristine samples that were measured were pressed under pressure of 19.5 MPa. Measurements were taken in both the perpendicular and parallel directions to the pressing direction. Parallel or perpendicular measurement refers to the measurement that was done on the length of the sample which was cut along either the parallel or perpendicular direction in relation to the pressing direction.

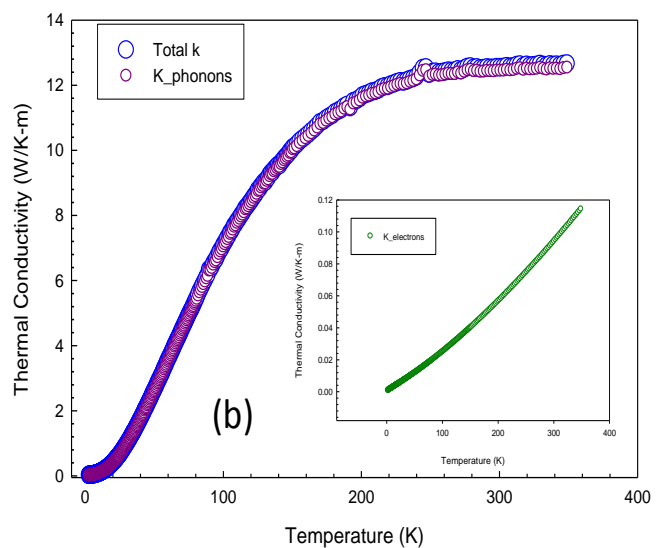
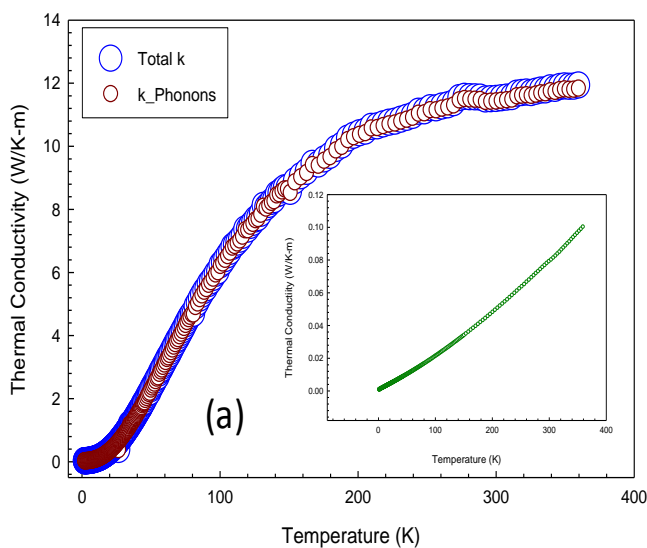


Figure 4.3: Pristine total thermal, phonon and electronic conductivity of samples pressed at 19.5 MPa and measured (a) parallel and (b) perpendicular to the pressing direction, (insert) is electrons contribution to total thermal conductivity.

Figure 4.3 contains the pristine data with the aim of showing the two contributions to thermal conductivity that are normally found. Total conductivity is written as follows:

$$K_{tot}(T) = K_e(T) + K_p(T) \quad (4.9)$$

where K_e is the electronic contribution which is calculated using equation 2.1 and K_p is the phonon contribution.

The electronic contribution is minimal, which is expected of graphitic material as shown in the inset to Figure 4.3. It is clear that phonon contribution is dominating throughout as compared with the total thermal conductivity. Furthermore, the direction of measurement has no effect on the total conductivity since the orders of magnitude of total conductivity are comparable. The electron contribution of this composite is much visible at a low temperature of less than 1 K as compared to 3 K suggested by Bowman et al for different graphite [2]. The low temperature contribution of electrons is subject to the scattering processes as temperature increases. There are various scattering processes that lead to this reduction, such as electron-electron, phonon-electron and phonon-phonon, including boundary scattering. The availability of non-graphitic regions also contributes to the decrease in the electron contribution which is seen more at low temperature and in the total conductivity through scattering processes and structure as observed by Klein and Holland [3].

4.2.2.2 Irradiated Data

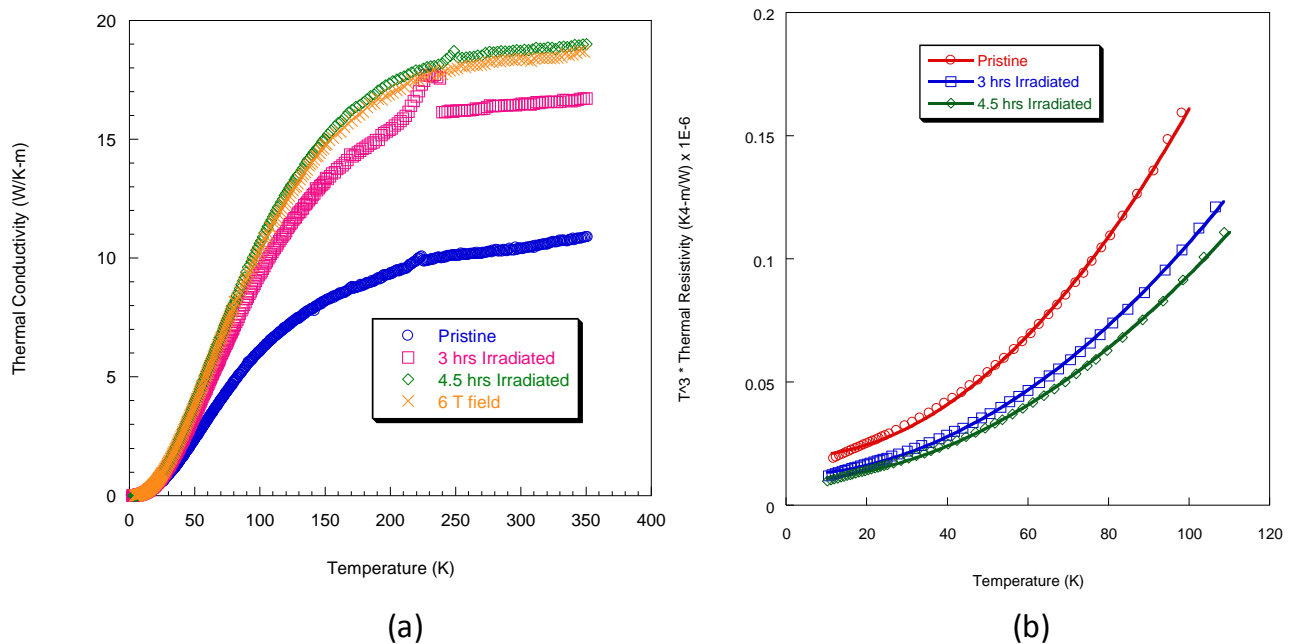


Figure 4.4: (a) Thermal conductivity and (b) thermal resistivity of the sample pressed at 19.5 MPa measured parallel to the pressing direction.

Figure 4.4(a) shows a comparison of the anomalous behaviour with regard to thermal conductivity of the pristine sample and the samples irradiated for 3 and 4.5 h. This includes measurements taken in the presence of an external magnetic field of 6 T along the length of the sample for the 4.5 h irradiated sample. Thermal conductivity is observed to increase with irradiation dose, which is anomalous behaviour. Under normal circumstances the thermal conductivity should decrease when the solid material is subjected to irradiation since irradiation induces defects within the material which would act as scattering centres for both the phonons and electrons responsible for thermal conductivity.

In order to understand what could be the cause of this anomalous behaviour of our samples, we used the approach of Hove and Smith [1]. They employed a two-media approach for the samples they considered, consisting of non-graphitic carbon (pitch binder) and a graphitic region. Our samples fit this model very well since they are graphite composites consisting of two regions: a non-graphitic phenolic resin as a binder, and a graphitic region consisting of

natural and synthetic graphites. These two regions can be taken in series for their contributions to total thermal conductivity. In order to treat the serial contribution of these two regions to the total thermal conductivity properly, it is convenient to examine the total thermal resistivity which is represented by equation 4.8. Figure 4.4(b) shows the thermal resistivity of the composite pressed at 19.5 MPa, with measurements taken along the length of the sample, cut parallel to the pressing direction. The solid lines through the data are fits to the data using equation 4.8 up to 120 K where such fits are valid and they start to deviate at high temperatures. Similar behaviour for both thermal conductivity and thermal resistivity is observed for the sample whose length was cut perpendicular to the pressing direction, as shown in figure 4.5. These results clearly show that thermal conductivity is independent of the flakes alignment, which will be aligned perpendicular to the pressing direction.

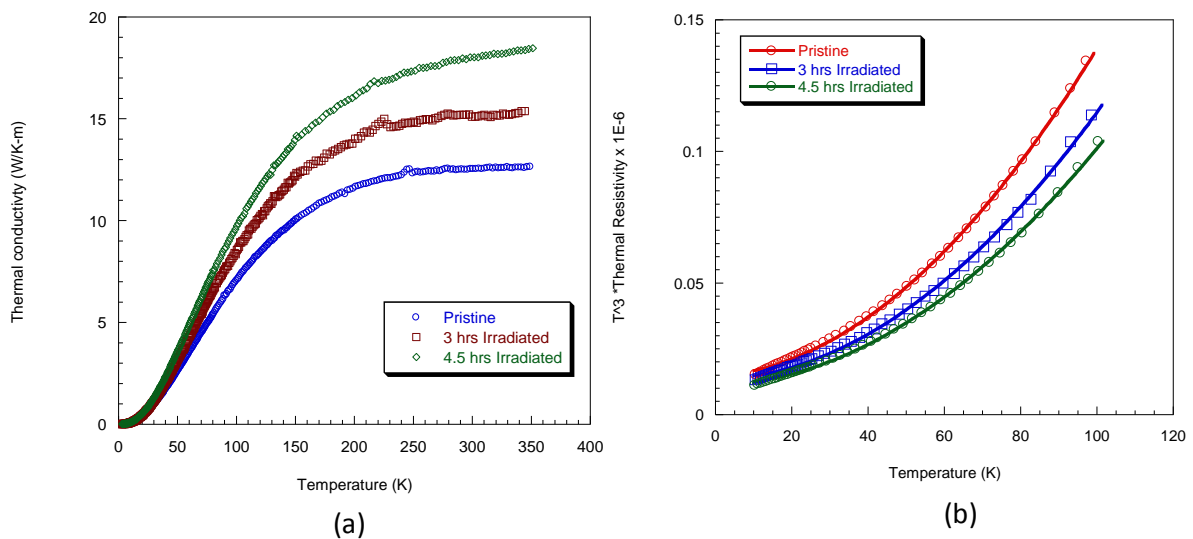


Figure 4.5: (a) Thermal conductivity and (b) thermal resistivity of high-pressure sample measured perpendicular to the pressing direction

Figure 4.6 shows the thermal conductivity of sample that was pressed at 10 MPa for comparison with both the pristine and irradiated samples. This sample was found to have a much higher porosity of 40% as compared with the sample pressed at 19.5 MPa which had a porosity of 25%. It can be seen in the figure that the thermal conductivity still increases with increasing irradiation dose since the values for both pressures are comparable. This shows the

validity of the assumption made by Hove and Smith that the effects of void spacing, which exist predominantly in the non-graphitic region, can be neglected.

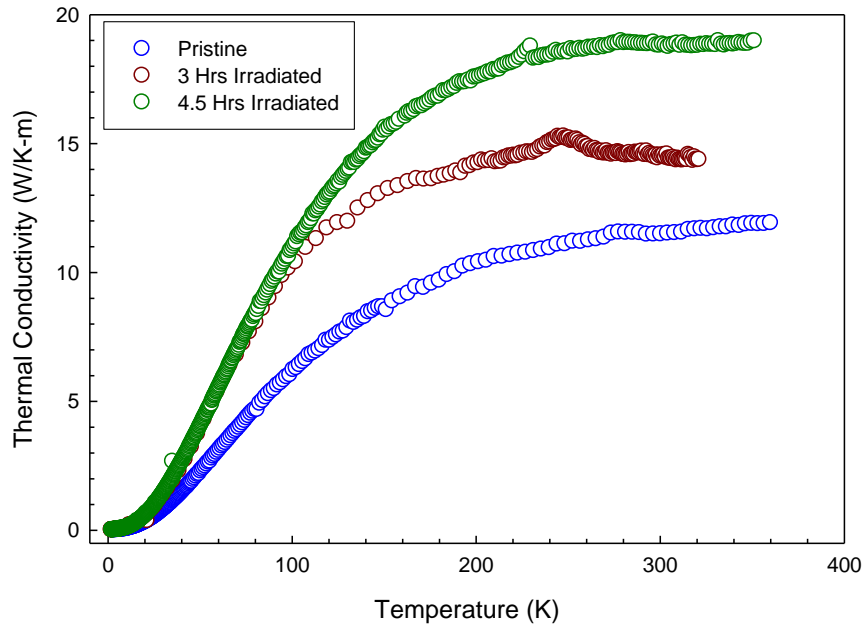


Figure 4.6: Thermal conductivity of lower-pressure (10 MPa) graphite composite measured along the perpendicular direction with respect to the pressing direction.

Table 4.2: Comparison of the average distance (l_3) between graphitic regions

Samples	Parallel direction (arb units)	Perpendicular direction (arb units)
Pristine	902	1 252
Irradiated for 3 h	1 492	1 364
Irradiated for 4.5	1 776	1 635

There are three important parameters that can be extracted from the fit using equation 4.8 to the data, namely, the path of constant scattering of phonons in the non-graphitic region (l_3) and concentration of defects (Ng). Table 4.2 shows crude extracted values of l_3 from the fit for both the parallel and perpendicular directions. The trend that appears here is that the non-graphitic mean free path increase with increasing irradiation dose. Since this distance is equivalent to the distance that the particle will travel within graphitic region which is crystalline shows that there is improvement of crystal structure with increasing irradiation dose. Then this support the observation that thermal conductivity increases with the irradiation dose. This is also observed in the both Raman and XRD data where it was observed that D peak from Raman which is associated with disorder became less with irradiation dose increase and the XRD peaks were much sharper for irradiated samples as compared to pristine sample.

In order to understand what could be the cause of the improvement in thermal conductivity brought about by irradiation using protons with energy of 2 MeV and fluences ranging from 10^{12} to 10^{14} protons/cm², corresponding to 3 and 4.5 h irradiation time, both the electrical resistivity and the Seebeck coefficient were considered. These give information about the response of the charge carriers in the sample, in both the zero and finite external magnetic fields.

4.3 ELECTRICAL CHARACTERISATION

Electrical characterisation was done on the graphite composite in order to develop a detailed understanding of the electronic properties of the sample.

4.3.1 ELECTRICAL RESISTIVITY

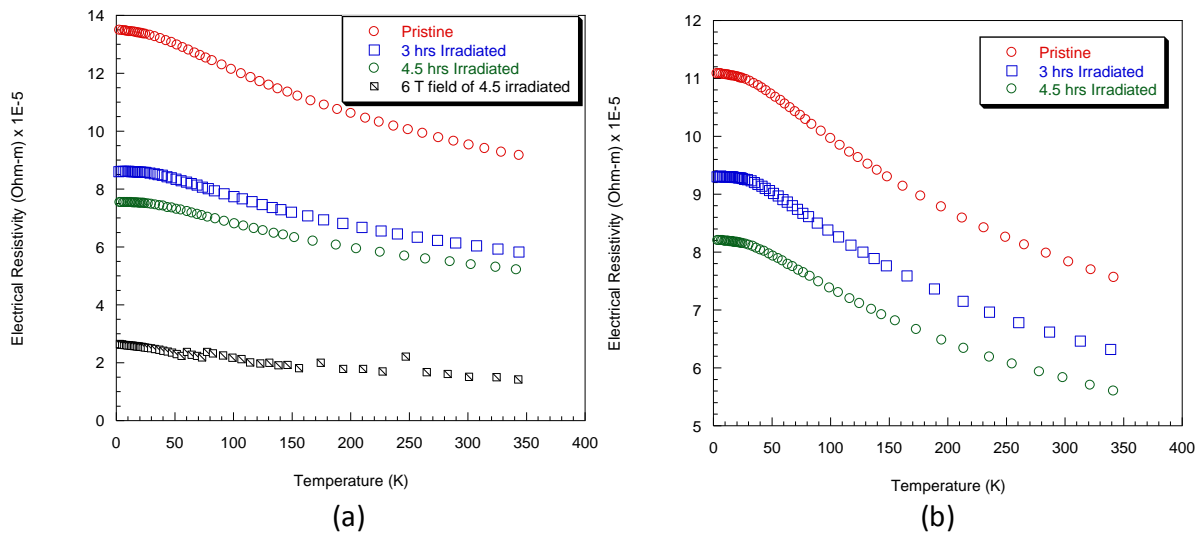


Figure 4.7: Electrical resistivity of sample subjected to 19.5 MPa pressure measured (a) parallel and (b) perpendicular to the pressing direction.

Figure 4.7 shows the electrical resistivity of samples measured in both parallel and perpendicular directions to the pressing direction. The pristine sample in both figures 4.7 (a) and (b) shows high electrical resistivity as compared with the irradiated samples; this is also observed for the low-pressure samples. Electrical resistivity in the presence of the field (6 T) also follows the same trend of decreasing as seen in figure 4.7 (a). Thus, electrical resistivity is a measure of charge carrier scattering, which could be either holes or electrons. Decrease in this manner is not anticipated for irradiated samples, since irradiation is expected to induce more defects in the sample that should act as scattering centres. Hence, increase in resistivity should be observed [4]. The behaviour of resistivity of the samples is consistent with what is observed in the thermal conductivity which supports the fact that there is structural improvement of the materials with irradiation dose. The purity of the material can be estimated through the Residual Resistivity Ratio (RRR) [5], as shown in Table 4.3.

Table 4.3: Comparison of Residual Resistivity Ratio (RRR) for both low- and high-pressure samples

Samples	Low-pressure samples	High-pressure samples
Pristine	± 0.7075	± 0.7076
Irradiated for 3 h	± 0.7071	± 0.7049
Irradiated for 4.5 h	± 0.7133	± 0.7184

The application of the RRR gives a rough index of sample impurity. Moreover, the RRR values of the composite of approximately 0,71 are comparable to the 1.6 obtained for highly oriented pyrolytic graphite (HOPG) [5]. From Table 4.3 it is clear that the approximate impurity levels of the composite are constant. Irradiation did not have an effect on the impurity of the sample since the RRR values are comparable with the pristine values.

4.3.2 SEEBECK COEFFICIENT

The data presented in this section are for samples pressed at 19.5 MPa and measured in both the parallel and perpendicular directions to the pressing direction. Furthermore, a measurement in the presence of an external magnetic field of 6 T has been included for the 4.5 h irradiated sample.

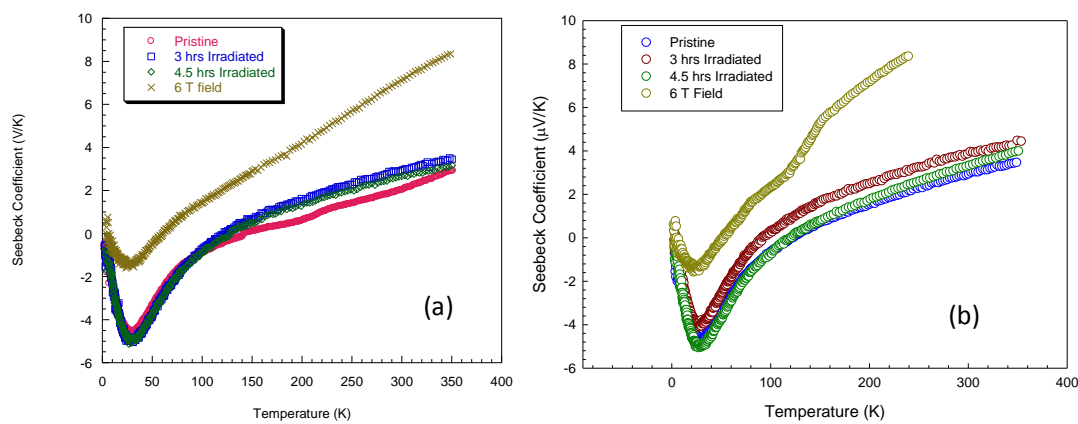


Figure 4.9: Comparison of Seebeck coefficient of high pressure measured both (a) parallel and (b) perpendicular to the pressing direction.

In figure 4.9 we observe the Seebeck coefficient, also referred to as thermopower, measured in both the parallel and perpendicular directions to the pressing direction. Typical behaviour of the Seebeck coefficient of graphite is that there is a dip around 35 K [6] which is noted in both cases in figures 4.9(a) and (b). The dip observed is normally attributed to phonon drag. The size of the dip is almost comparable to that of most graphite samples. What is striking here is the shift of the data when a magnetic field is applied, we then see most of the negative part of the Seebeck coefficient (which is associated with electrons) decrease quite substantially at the expense of an increase in the positive part (which is attributed to holes). Since thermoelectric power depends on the carrier concentration difference $N_e - N_h$, where N_e and N_h denote electron and hole density, and hence the observed shift would mean that the majority carriers responsible for the thermo power will be holes in this case.

REFERENCES

1. Hove, J.E. and A.W. Smith, Phys. Rev., (1956). **104**: p. 892-900.
2. Bowman, J.C. and J.A. Krumhansl, J. Phys. Chem. Solids., (1958). **6**: p. 367-379.
3. Klein, C.A. and M.G. Holland, Phys. Rev., (1964). **136**: p. 575-590.
4. Smith, A.W. and N.S. Rasor, Phys. Rev., (1956). **104**: p. 885-891.
5. Kaburagi, Y. and Y. Hishiyama, Carbon, (1998). **36**: p. 1671-1676.
6. Ayache, C., A.d. Combarieu, and J.P. Jay-Gerin, Phys. Rev. B, (1980). **21**: p. 2462-2465.

CHAPTER 5: CONCLUSION

Irradiation of a solid is known to induce defects within that solid, which affects both its structural and thermal properties. In this study the graphite composite exhibited anomalous behaviour after irradiation. It was observed that the D-peak in Raman spectroscopy, which is sensitive to defects, decreases with irradiation. Furthermore, structural characterisation with XRD showed a pattern of increasing average crystallite sizes. This indicated some form of structural improvement.

In thermal characterisation of the material, a similar trend was observed in that thermal conductivity increased with irradiation. This trend was seen to be independent of both the uni-axial moulding pressure of the samples and the direction of measurement with respect to moulding pressure. An external magnetic field of 6 T was applied to the 4.5 h irradiated sample but had no effect on increasing conductivity. However, to understand this data we used the theory proposed by Hove and Smith [1], who looked at graphite consisting of two regions: non-graphitic (binder) and graphitic regions. This model of graphite correlates well with the graphite composite used for this study. Taking the two graphite regions in series, the thermal resistivity was investigated. It was found that the data obtained fitted well with equation 4.8, which represents the theory proposed. The theory has led to the conclusion that the behaviour of the graphite composite can be attributed to structural improvement, which occurs with irradiation. The parameters, such as average crystallite size and constant scattering path in the non-graphitic region, are in fair agreement with those found for various other graphites by Hove and Smith [1].

The electrical resistivity of the pristine samples was noted to be high compared with that of the irradiated samples. This was also unexpected since irradiated graphite material is expected to have more scattering centres and hence an increase in electrical resistivity. The Residual Resistivity Ratio (RRR) showed that impurities within the material are minimal and are consistent regardless of irradiation. Thus irradiation did not introduce any impurities within the material. The Seebeck coefficient, on the other hand, showed the expected dip for graphite material, which is attributed to phonon drag at 35 K. However, since thermopower depends on the electrons and the hole density, what was observed supports a possibility of hole doping after irradiation.

Reference

- [1] Hove, J.E. and Smith, A.W. (1956). *Phys. Rev.*, **104**: 892–900.